Highlights

Enhancing measurement precision of superluminescent diode-based chromatic confocal sensor by real-time spectral correction

Lóránt Tibor Csőke,Szabolcs Károly Kautny,Zsolt Kollár

- High-brightness chromatic confocal sensor with reference beam
- Dual-beam spectrometer architecture
- High-performance optical surface profiling system

Enhancing measurement precision of superluminescent diode-based chromatic confocal sensor by real-time spectral correction

Lóránt Tibor Csőke[a,b,*], Szabolcs Károly Kautny[a] and Zsolt Kollár[b]

[a]Optimal Optik Ltd., Dayka Gábor utca 6/b, H-1118 Budapest, Hungary

[b]Department of Artificial Intelligence and Systems Engineering, Faculty of Electrical Engineering and Informatics, Budapest University of Technology and Economics, Műegyetem rkp. 3., H-1111 Budapest, Hungary

ARTICLE INFO

Keywords:
chromatic confocal sensor
optical surface profiling
dual-beam spectrometer
superluminescent diode based sensor

ABSTRACT

Chromatic confocal sensors are widely used in high-resolution, non-contact distance measurements. Despite their advantages, conventional implementations often suffer from low light utilization efficiency and instability in the illumination spectrum, both of which degrade measurement accuracy, particularly when using broadband semiconductor sources such as superluminescent diodes. In this study, we address these limitations by introducing a chromatic confocal system that incorporates a high-brightness SLD alongside a real-time spectral correction mechanism. The proposed optical setup features a dual-beam spectrometer capable of simultaneously capturing the reflected axial intensity signal and the intrinsic spectrum of the light source using a global shutter camera. This architecture enables frame-by-frame normalization of the measured signal, reducing the impact of spectral fluctuations and inherent source nonuniformities. Simulation and experimental results demonstrate that, in the previously introduced system, this method reduces the wavelength-to-distance encoding error from ~~approximately ±~~0.4 µm to below 0.2 µm, and decreases distance uncertainty due to source instability by ~~nearly~~ 20%. The system is particularly suited for applications involving low-reflectivity surfaces or requiring high-speed scanning at rates up to tens of kHz.

1. Introduction

Chromatic confocal (CC) sensors provide precise, non-contact distance measurements and are widely used in surface profiling and optical distance sensing applications. These sensors operate based on the principle of chromatic aberration, utilizing the wavelength-dependent focal shift to achieve high-resolution axial measurements [1]. By focusing light of different wavelengths from a broadband source through a dispersive objective lens, CC sensors can cover extended axial measurement ranges from the µm to mm scale [1]. Their key advantages include high measurement accuracy, rapid response time, and excellent stability, making them well-suited for displacement and thickness measurements at sub-µm resolution [2]. CC sensors are employed across diverse fields, such as ultra-precision machining, industrial and medical surface topography analysis, and spectral reflectance characterization [3, 4, 5, 6, 7, 8].

Advances in spectral multiplexing have enabled the parallel evaluation of multiple lateral points, thereby increasing the throughput of CC systems [9]. Additionally, the integration of diffractive optical elements or actuated pinhole arrays has significantly enhanced both the speed and performance of CC sensors, facilitating "single-shot" three-dimensional imaging [10, 11, 12].

In our previous publication, we identified a key limitation of CC sensors: their inherently low light utilization efficiency due to an etendue mismatch between the light source and the confocal optical system [13]. This mismatch results in a loss of more than four orders of magnitude in the emitted radiant power from the source. As less light reaches the sample surface, the amount of reflected light collected by the system is reduced, leading to a substantial degradation in the signal-to-noise ratio (SNR), particularly when examining low- or diffusely reflecting samples. To overcome this limitation, we previously proposed a novel CC system employing a fiber-coupled superluminescent diode (SLD), which offers a much smaller etendue – and thus significantly higher power density – than conventional light sources such as light-emitting diodes (LED). In this setup, the SLD delivers an input power of 20 mW into a 4.4 µm single-mode fiber, resulting in orders of magnitude higher power density compared to an LED [13]. Both theoretical analysis and experimental validation have shown that the light utilization efficiency of the SLD-based CC system can approach 100 %, with remaining losses primarily attributed to the fiber optic connections [13].

For CC sensors, the ideal illumination source would possess a perfectly flat and temporally stable spectrum. However, many semiconductor-based sources, such as LEDs and SLDs, often exhibit spectral peaks in their emission profiles, depending on the specific underlying technology. To broaden the emission bandwidth of SLDs, multiple quantum well structures are typically employed, which frequently result in two prominent spectral peaks [14]. The inherent spectral shape and noise characteristics of the illumination spectrum directly influence the intensity distribution at the focal spot, and consequently affect the measured axial intensity signal (AIS). This leads to increased uncertainty in peak determination and distance decoding. Several publications have addressed this issue from a signal processing perspective [15, 16, 17]. Although advanced algorithms have

*Corresponding author
csoke.lorant@edu.bme.hu (L.T. Csőke)
http://www.mit.bme.hu/general/phd/csoke (L.T. Csőke)
ORCID(s):

been developed to extract distance information from the AIS – focusing on improving height measurement accuracy and noise suppression while maintaining acceptable processing speeds – none of these works explicitly address the problem at the hardware level [18, 19, 20].

Using an SLD as a light source in a CC system can substantially enhance signal intensity, but its inherent spectral instability can significantly compromise measurement accuracy. These spectral fluctuations are primarily caused by back-reflections entering the SLD chip, which are amplified by the high optical gain within the cavity [21, 22, 23]. A common mitigation strategy involves placing an optical isolator immediately after the SLD – such as the IO-F-SLD150-895 from Thorlabs Inc. [24] – to prevent reflected light from propagating back into the source. This component effectively blocks reflections originating from various elements and interfaces within the optical system, thereby reducing the risk of spectral peaking or unintended lasing effects.

However, even in the absence of back-reflections, spectral noise may persist due to intrinsic noise mechanisms in semiconductor devices. These include thermal noise, $1/f$ noise, shot noise, and –specifically in the case of SLDs – residual internal reflections [25, 26, 14]. Additionally, variations in the SLD chip temperature or drive current – often introduced to adapt to differing sample reflectance – can lead to significant, nonlinear distortions in the spectral shape. This dynamic behavior of the light source spectrum renders conventional compensation methods, such as capturing a single reference spectrum prior to measurement, ineffective. Therefore, while the inclusion of an optical isolator is effective in suppressing reflection-induced resonances, it does not eliminate all forms of spectral instability.

This study, therefore, aims to investigate the impact of such spectral disruptions on peak extraction accuracy and noise in the computed distance, using simulation-based analysis and experiments. To address these challenges, we propose a novel solution that introduces an optical system capable of capturing both the intrinsic spectrum of the light source and the reflected AIS simultaneously. This is realized through a custom dual-beam spectrometer architecture employing a global-shutter camera to record two spectra in parallel. The associated signal processing workflow is extended by normalizing the AIS with respect to the simultaneously acquired reference spectrum. This real-time spectral correction approach effectively mitigates noise and nonlinearity in the measured distance, thereby improving the robustness and accuracy of peak detection algorithms. In our study, we demonstrate that the non-linearity error in the estimated wavelength-to-distance encoding can be reduced from ~~approximately~~ $\pm 0.4\,\mu m$ to below $\pm 0.2\,\mu m$ scale, and that the distance measurement uncertainty caused by light source fluctuations can be decreased by a factor of ~~approximately~~ 20%. In this context, it is also important to note related work on alternative CC implementations. For instance, Liu *et al.* recently demonstrated a CC measurement method employing a phase Fresnel zone plate (FZP) as the dispersive element [27]. Their approach achieves a large axial measurement range of over 16 mm and an axial resolution of $0.8\,\mu m$, with high displacement measurement accuracy better than 0.4%. In contrast to our refractive, multi-element objective, the FZP-based system emphasizes simplicity and cost-effectiveness, while also comparing peak extraction algorithms, where Gaussian fitting yielded the best accuracy. By comparison, our work targets high-NA objectives and dual-spectrum acquisition for reference-based compensation, with particular focus on reducing noise-induced localization errors. Together, these studies highlight complementary directions in the development of chromatic confocal systems: low-cost, diffractive designs optimized for large measurement ranges versus high-precision, noise-resilient architectures incorporating reference channels.

The structure of the paper is as follows: Section 2 presents the spectral model of the proposed CC system equipped with a reference detector. Based on this model, the impact of spectral instability and the inherent spectral shape of the light source on the performance of various peak extraction algorithms is investigated through simulations. In Section 3, a practical implementation of the proposed custom optical system is described, and experimental results are provided for comparison with simulation outcomes. Finally, Section 4 discusses the technological significance and practical implications of the findings and provides an outlook on the remaining challenges to resolve.

2. Simulation

Two main aspects are to be addressed in the analysis of how non-ideal spectral characteristics of the light source impact the signal processing chain in CC systems, namely the intrinsic shape of the spectrum and the intensity fluctuations at each wavelength. While in short term, the first one could be treated as a systematic error to the peak estimation – one could capture the spectrum prior measurements and compensate the AIS with its shape –, the latter accounts for a significant factor in distance measurement noise. Excluding sample-specific effects and optical aberrations, the objectives of the simulation framework are as follows:

- **Sensitivity to spectral noise and shape:** The influence of additive spectral noise on peak localization uncertainty is analyzed, along with the effect of shape distortions in the illumination spectrum on absolute precision. Spectral regions within the AIS signal that are most sensitive to such perturbations are identified, and their contribution to bias in peak estimation is assessed.
- **Modeling limitations and real-world considerations:** Discuss limitations of the simulation framework, including effects such as stray reflections, mode couplings in the optical fibers, temperature dependence, or detector nonlinearity that may not be fully captured in the model. Highlight how these factors may impact the generalizability of the proposed methods to experimental systems.

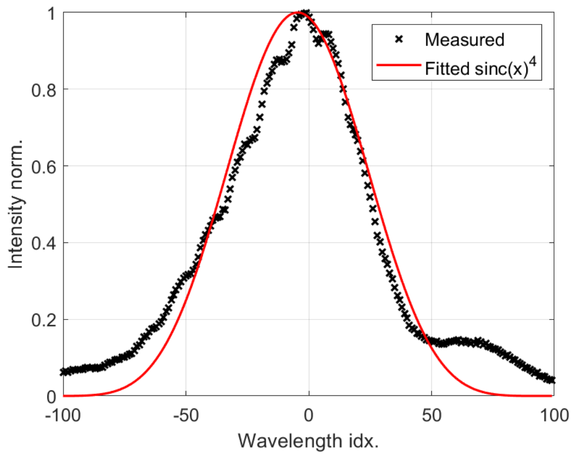

Figure 1: Measured AIS signal with a least-squares fit using a $\mathrm{sinc}(x)^4$ function. Aberrations of the actual signal, including a small right-side lobe, are clearly visible.

2.1. Spectral signal model

Multiple signal models have been proposed for CC sensors since the introduction of confocal scanning microscopy. Some studies derive the system response from electromagnetic diffraction theory, following the framework established by Richards and Wolf [28, 29], while others employ a simplified $\mathrm{sinc}(x)$-like spectral model, as introduced by Wilson and Sheppard [30, 31, 15]. With the availability of modern simulation tools such as *Zemax OpticsStudio* or *MATLAB*, it has become feasible to incorporate optical aberrations and sample properties, including tilt, reflectivity, or roughness, into the response model [32, 15, 16]. Regardless of the modeling approach, the common objective is to accurately extract depth information from the detected spectral signal.

The measured response of a CC sensor typically appears as a localized spectral peak characterized by a centroid position, peak intensity, and full width at half maximum (FWHM). In practice, the signal may exhibit distortions such as asymmetry, peak flattening, or side lobes as illustrated in Figure 1. These effects necessitate the use of robust fitting functions to minimize residual error and reliably estimate the peak position. The estimated peak wavelength $\hat{\lambda}_z$ can then be converted to an axial distance using a pre-calibrated wavelength-to-distance mapping function, $\hat{z} = f(\hat{\lambda}_z)$, obtained through reference measurements with a high-precision positioning system.

The signal model for the simulations was chosen to isolate optical aberrations and sample-specific characteristics from the effects of source non-idealities. To this end, a simplified $\mathrm{sinc}^4(x)$-based response function H_{CC} is used for signal generation as follows:

$$H_{CC}(\lambda_i, z) = \mathrm{sinc}\left(\frac{\lambda_i - \lambda_z}{\alpha}\right)^4 \tag{1}$$

Here, λ_i denotes the discrete wavelength index detected by the spectrometer, λ_z is the ideal peak wavelength corresponding to axial position z, and α is a width parameter characterizing the spectral response of the system. The function $\mathrm{sinc}(x)$ is defined following MATLAB's convention as $\mathrm{sinc}(x) = \sin(\pi x)/\pi x$. The value of α was determined by fitting Eq. 1 to experimentally measured AIS. In this work, a value of $\alpha = 100$ was selected based on the results of this empirical calibration.

For peak fitting, a Gaussian model is employed, based on Eq. 2, following Caruana's method as described by Guo [33].

$$\hat{I}(\lambda_i, z) = A \cdot \exp\left(-\frac{(\lambda_i - \hat{\lambda}_z)^2}{2\sigma^2}\right) \tag{2}$$

where A is the amplitude, $\hat{\lambda}_z$ is the estimated peak wavelength corresponding to axial position z, and σ is the standard deviation of the Gaussian function.

The final detected AIS, denoted $I_{\mathrm{AIS}}(\lambda_i)$, is modeled as the product of the chromatic objective's spectral transfer function Eq. 1 and the light source spectrum $I_S(\lambda_i)$, assuming all other components in the optical path (fibers, splitters, attenuators, detectors, sample reflectance, etc.) exhibit ideal spectral transfer characteristics, i.e., $H(\lambda_i) = 1$.

2.2. Impact of source spectral shape on fitting and calibration

First, we examine how the inherent spectral shape of the light source affects the accuracy of distance–wavelength calibration, while neglecting noise for clarity. As discussed in the previous section, the detected AIS signal results from the product of the confocal objective's response function and the spectrum of the illumination source. This combined effect functions as an optical bandpass filter, whose center wavelength shifts with the sample distance. Figure 2 shows simulated AIS curves under the assumption of an ideal, lossless optical system and a perfectly reflecting sample. The light source spectrum I_s was modeled with a dual-peak shape, similar to that of SLDs, to better approximate the characteristics of the prototype system introduced later. The modulation effect introduced by I_s is clearly evident in the shape of the AIS signals.

Before a CC system can be used for distance measurements, the dispersion relation must be determined through calibration. This is typically achieved by scanning a precisely aligned mirror surface over a known distance range and recording the detected peak position at each step using a high-accuracy distance measuring device, such as an interferometer. A polynomial is then fitted to the resulting dataset and used as the calibration equation to convert detected peak positions into absolute distance values.

However, if the illumination spectrum exhibits a non-uniform intensity distribution, the resulting AIS signal becomes distorted. These distortions cause the detected peak position to deviate from its ideal location, introducing nonlinearity into the wavelength–distance mapping. While polynomial fitting can compensate for some of this nonlinearity,

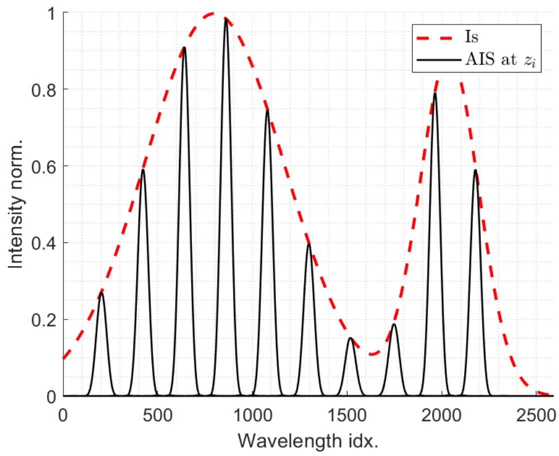

Figure 2: Simulated AIS signals at different z_i positions, assuming linear dispersion and a dual-peak spectral shape representative of an SLD light source.

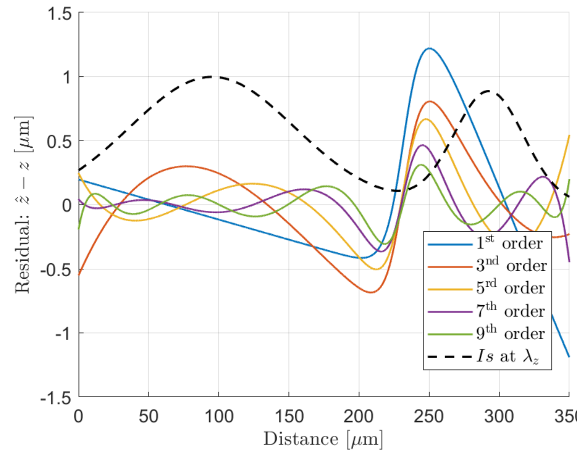

Figure 3: Calibration error resulting from fitting polynomials of various orders to the simulated wavelength–distance dataset.

it may not fully capture the distortion. In such cases, a residual systematic error remains in the measurement. This error can be mitigated by increasing the polynomial order, but doing so increases the risk of overfitting and reduces robustness.

To study this effect, a simulation was performed using MATLAB. A synthetic spectral signal was generated using 2592 wavelength bins based on real SLD spectral data. A dual-peak exponentially modified Gaussian (DP-EMG) curve was fitted to the actual captured spectrum (the mathematical model is provided in Appendix A). A theoretical dispersion relation was then defined, mapping a 350 µm distance range into 2200 wavelength bins, in accordance with the observed characteristics of the prototype system.

A total of 1000 AIS curves were generated across the 350 µm range using Eq. 1, with central wavelengths determined by the dispersion relation. These AIS signals were then modulated by the artificial I_s curve to simulate the effect of the light source spectrum. Peak detection was applied to each AIS curve using Eq. 2, and the resulting peak positions were used to fit polynomials of various orders to the ground-truth displacement vector z. These fitted equations were then used to estimate $\hat{z}$ from the detected peaks, and the residual errors $\hat{z} - z$ were calculated and plotted.

As shown in Fig. 3, increasing the polynomial fitting order reduces the calibration error. However, even at high orders (e.g., 9th order), residual errors on the order of ± 0.3 µm persist. While further reduction in error is possible using lookup tables and advanced interpolation methods, such techniques are more computationally intensive and may not fit the speed requirements of the measuring system.

Additionally, variations in the illumination spectrum due to aging, temperature fluctuations, or drive current instability cannot be handled by this static calibration method. In such cases, recalibration becomes necessary. However, this process requires precise instrumentation, accurate alignment, and results in system downtime. Moreover, even with regular recalibration, short-term spectral fluctuations may still introduce uncorrected errors. To assess the impact of such instabilities and several noise sources, additional simulation trials were conducted in the following section.

2.3. Sensitivity of peak estimation to source spectral noise

This section presents a numerical and analytical evaluation of the probability that a chromatic confocal sensor incorrectly identifies the location of the spectral peak, denoted as $\hat{\lambda}_z$, in the presence of additive Gaussian noise.

The underlying signal model assumes a flat illumination spectrum modulated by the axial response of the system, which follows a sinc^4 shape centered around the true peak. The sensor samples the spectrum over $N_\lambda = 201$ discrete wavelengths $\{\lambda_i\}$ spanning a normalized range $[-\alpha, \alpha]$, with $\alpha = 100$. Gaussian noise with mean $\mu_N = 0$ and standard deviation $\sigma_N = 0.1$ is independently added to each spectral channel.

Two complementary methods are employed to quantify the probability $P(\hat{\lambda}_z = \lambda_i)$ that the system identifies index i as the spectral maximum:

1. **Monte Carlo simulation:** A large number of noisy realizations ($N_{\text{meas}} = 10^6$) of the modulated spectrum are generated, and the peak index is recorded for each trial. The empirical detection probability is obtained by normalizing the histogram of detected peak positions.
2. **Analytical integration:** For each candidate index λ_i, the detection probability is expressed as a multivariate integral (derived in Appendix B):

$$P(\hat{\lambda}_z = \lambda_i) = \int_{-\infty}^{\infty} f_i(t) \prod_{j \neq i} F_j(t)\,\mathrm{d}t, \tag{3}$$

where $f_i(t)$ and $F_j(t)$ are the Gaussian probability density function (PDF) and cumulative distribution function (CDF), respectively, evaluated at the wavelength

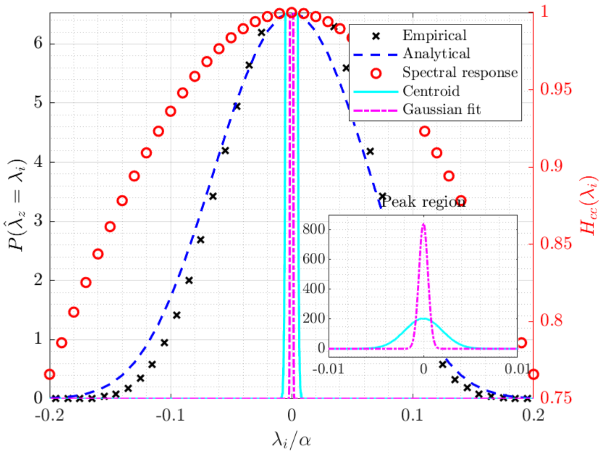

Figure 4: The system's spectral transfer function and the resulting probability distributions for three localization methods: maximum index detection, in which the wavelength index corresponding to the highest intensity is selected as the peak, centroid estimation, and Gaussian curve fitting. For the maximum detection method, both empirical Monte Carlo results and the corresponding analytical prediction from Eq. 3 are presented. Label definitions: *Empirical* denotes Monte Carlo simulations of maximum index detection; *Analytical* corresponds to Eq. 3; *Centroid* and *Gaussian fit* represent Monte Carlo simulations based on centroid calculation and Gaussian fitting, respectively.

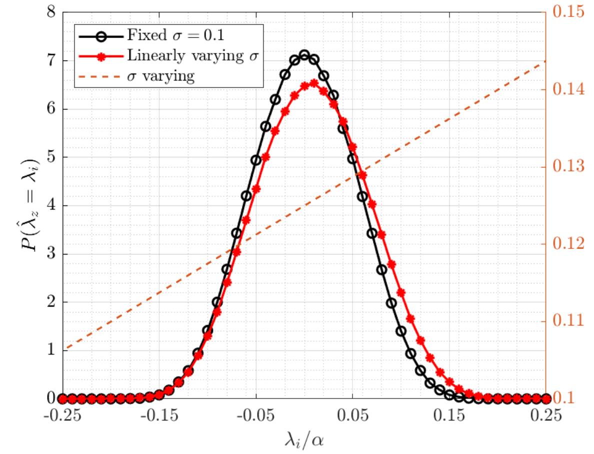

Figure 5: Effect of wavelength-dependent intensity noise on peak localization, simulated using 10^6 Monte Carlo trials.

index λ_j. The mean signal μ_j at each index is given by the deterministic sinc^4 spectral response, and the noise standard deviation σ_j is assumed uniform across wavelengths. This integral quantifies the probability that the signal at λ_i exceeds all others, accounting for both the spectral modulation and the stochastic nature of the additive noise.

Both methods yield a probability distribution over the wavelength axis, quantifying the likelihood that noise causes incorrect peak detection. The spectral transfer function and the resulting detection probability distributions for various noise levels are illustrated in Figure 4.

The analytical results presented above are valid under the assumption of uncorrelated additive Gaussian noise with known per-channel means μ_i and standard deviations σ_i. However, in practice, the illumination spectrum may exhibit correlated variations, leading to interdependence between adjacent spectral channels.

To account for this, a more general formulation can be derived using the theory of multivariate normal distributions. In this case, the probability that the maximum occurs at the index k corresponds to the so-called orthant probability. Specifically, we define a transformed random vector $\mathbf{Z}_k$ such that:

$$P(X_k = \max X_i) = P(\mathbf{Z}_k > 0) = \int_{\mathbb{R}_+^{N-1}} \mathcal{N}\left(\mathbf{z};\, \mathbf{C}_k\boldsymbol{\mu},\, \mathbf{C}_k\boldsymbol{\Sigma}\mathbf{C}_k^\top\right) d\mathbf{z}, \tag{4}$$

where $\mathbf{C}_k$ is a contrast matrix that encodes all pairwise differences between the channel k and the others, and $\boldsymbol{\Sigma}$ is the full noise covariance matrix.

Equation (4) expresses the probability that all elements of $\mathbf{Z}_k$ are positive—i.e., that channel k exceeds all others. This is known as the orthant probability of a multivariate Gaussian distribution. While no closed-form solution exists for $N > 3$, efficient numerical methods have been developed, including the algorithms of Genz and Bretz [34, 35], as well as Monte Carlo sampling techniques. The derivation of this expression, including the construction of the contrast matrix $\mathbf{C}_k$ and the transformation of the covariance structure, is provided in Appendix C.

For more complex peak detection algorithms such as centroid estimation or curve fitting (e.g., Gaussian fitting), the expressions above become either analytically intractable or computationally prohibitive. These methods produce real-valued estimates rather than discrete maxima, and require evaluating the distribution of nonlinear functionals of the random signal. When the noise covariance is large and high-dimensional, the corresponding integrals span dozens of dimensions, making direct evaluation impractical.

A practical alternative is to estimate the uncertainty through Monte Carlo simulations. This approach was employed here as well: we computed the centroid and performed Gaussian curve fitting to the noisy signal, repeating the procedure over many trials. The resulting distributions of estimated peak positions were analyzed and compared. Figure 4 shows how the probability distribution of peak localization changes under centroid-based and curve-fitted estimation compared to simple maximum detection, using the same simulation framework described above. Notably, the width of the probability distribution is nearly two orders of magnitude narrower than in the case of maximum detection, indicating significantly lower noise sensitivity in the fit-based localization processes.

The influence of wavelength-dependent noise variance on peak localization was investigated using the maximum detection method. To model this effect, a non-uniform noise level was introduced across the spectral channels, with the noise standard deviation σ increasing linearly toward longer wavelength indices. Figure 5 illustrates how this non-uniform noise variance distribution distorts the detected AIS signal. As expected, the varying noise level introduces asymmetry into the AIS spectrum: the imposed linear variance profile produces a broadened peak with an apparent shift toward the region of higher variance. This effect can be interpreted as a consequence of the broadened probability density functions of the detected intensity at each spectral channel. Because higher intensity fluctuations are more likely to occur on the side with increased variance, while the opposite side remains comparatively constrained, the simple maximum index detection method becomes biased. The results shown in Figure 5 are based on Monte Carlo simulations comprising 10^6 trials.

Such non-uniform distributions of intensity noise across the spectrum cause the detected peak position to deviate systematically from the actual spectral center. This behavior is particularly relevant for real-world light sources, where the noise power often scales with optical intensity due to spontaneous emission processes. In SLDs, regions of higher emission typically correspond to increased photon shot noise and amplified spontaneous emission (ASE) noise, both of which contribute to greater fluctuations [36, 37]. Figure 6 shows the measured standard deviation of intensity noise on the AIS and reference (REF) channels, obtained from 10 000 frames acquired with the prototype system at a sampling frequency of $f_s = 1$ kHz. The REF channel denotes a dedicated measurement path introduced as a novel approach for compensating source-related fluctuations in the measured signal.

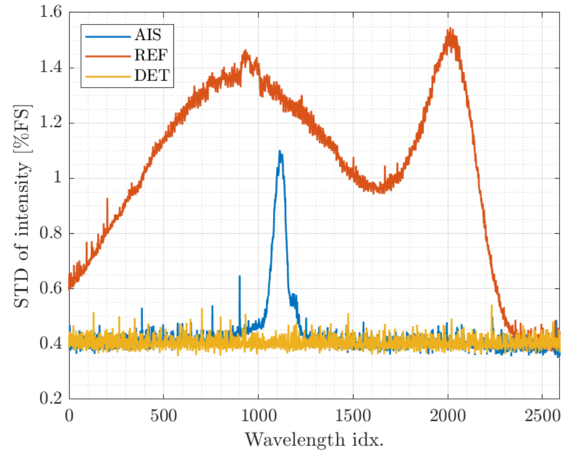

Figure 6: Measured standard deviation of intensity noise across the spectral channels in the prototype dual-beam spectrometer for the AIS and reference (REF) channels, together with the dark detector noise (DET). The elevated noise observed in high-intensity regions reflects the signal-dependent nature of photon shot noise and amplified spontaneous emission. All curves are normalized and displayed relative to the detector's full dynamic range of 10 bits, abbreviated as FS (full scale).

2.4. Simulation results and evaluation of correction methods

Simulation trials were conducted to evaluate the performance of different correction methods under varying ratios of illumination spectral noise and detector noise. Three peak detection strategies were considered: simple maximum detection, centroid calculation, and Gaussian fitting. The ratio of temporal variance of the light source to the detector noise variance was varied linearly from 0.1× to 10×, resulting in ten distinct SNR conditions. Each condition was tested over 10,000 simulated time samples.

The signal generation procedure was implemented as follows. A synthetic illumination spectrum $I_s(\lambda_i) \in \mathbb{R}^{N_\lambda}$ with $N_\lambda = 2592$ bins was generated using a flat spectral profile corrupted by additive white Gaussian noise. The AIS spectrum $\mathbf{y}_{\text{AIS}}$ was obtained by multiplying the illumination spectrum with a sinc^4-shaped system response centered at a fixed axial position $z_0 = 150\,\mu$m, simulating the axial response of a chromatic confocal objective. The reference signal $\mathbf{y}_{\text{REF}}$ was modeled as the unfiltered illumination spectrum, while independent Gaussian noise was added to both the AIS and REF channels to simulate other uncorrelated noise sources. The dispersion slope used in the simulations was determined from the theoretical optical model of the realized confocal objective and the spectrometer, exported from ZEMAX OpticStudio. The slope was defined as the ratio of the effective wavelength range to the full dispersion range of 350 µm. Based on the theoretical spectrum of the SLD and the spectrometer architecture, the effective wavelength range was found to correspond to 2100 pixels on the detector resulting in $\alpha = \Delta\lambda_i/\Delta z = 6$ pixels/µm).

Two signal correction methods were applied. The first was a simple point-wise division of the AIS signal by the reference signal. In the second method, the AIS signal was smoothed using an exponentially weighted moving average (EWMA), updated at each time step with a forgetting factor $\gamma = 0.5$, corresponding to a time constant $\tau = -1/\ln(\gamma) \approx 1.44$ samples.

Peak position estimation was performed using all three detection methods on both raw and corrected AIS signals. The signal region used for evaluation was selected as all points above 50% of the detected peak intensity. The standard deviation of the estimated peak positions was computed for each method and correction scheme across all SNR conditions. To express peak localization uncertainty in physical units, the resulting standard deviations were normalized by the dispersion slope defined above.

Figure 7 summarizes the results of the simulation study. The three subplots correspond to the different detection methods, while each plot shows the standard deviation of peak estimation under the various correction schemes. The x-axis represents the ratio of the illumination SNR to the detector SNR, i.e. $\text{SNR}_{\text{Illum}}/\text{SNR}_{\text{Det}}$. Here, $\text{SNR[dB]} = 10\log_{10}(1/\sigma^2)$, assuming unit intensity for the illumination spectrum. We define $\text{SNR}_{\text{Illum}}$ as the ratio of the ideal spectral signal level to the standard deviation of illumination noise added prior to the confocal filter, i.e. before multiplication with the confocal response function. In contrast, SNR_{Det} is defined as the ratio of the ideal signal level to the standard deviation of detector noise, which is added directly to the AIS signal after the confocal filtering stage. The ideal signal level is defined as unity. In the simulations, the detector SNR was fixed at 46 dB, while the illumination SNR was swept over the following values: 60.0, 38.4, 32.8, 29.4, 26.9, 25.0, 23.5, 22.2, 21.0, and 20.0 dB.

In the case of maximum position detection and Gaussian fitting, the raw AIS signal exhibits increased peak estimation variance when illumination noise dominates over detector noise. Conversely, when detector noise is the primary contributor, the raw signal yields better performance, and the estimation variances of all methods converge at the equal-noise point, defined by $SNR_{Illum} = SNR_{Det}$. The reference division method effectively suppresses source-spectrum-induced noise, maintaining nearly constant performance across varying SNR conditions. However, as detector noise becomes dominant, both the raw and EWMA filtered signals outperform the division method.

The centroid-based estimator was largely invariant to the applied correction methods. This behavior can be attributed to the fact that the centroid calculation depends primarily on the area under the AIS peak, which is less sensitive to the type of perturbations simulated here.

Although further investigation may be required for real-world applicability, the simulation results suggest that even simple correction schemes –such as division by the reference channel– can improve peak estimation accuracy, provided that the remaining parts of the detection chain (e.g., detectors, optics) introduce less noise and distortion than the illumination source itself.

It is important to note that this simulation study did not account for real-world effects such as channel gain mismatches between the AIS and REF channels, non-uniform reflectivity of the sample, optical aberrations, or non-uniform spectral noise in the light source. Some additional scenarios, such as linear and quadratic gain distortion of the reference signal, were considered based on manufacturer specifications of the fiber coupler [38], and were found to have a minor effect on the final results.

2.5. Modeling limitations and real-world considerations

We have investigated and simulated several scenarios to assess how noise and disturbances affect peak estimation accuracy in a CC sensor. The results demonstrate that the inherent spectral shape of the illumination source introduces nonlinearities into the calibration curve, leading to systematic errors in peak localization. This observation highlights a critical limitation: if the source spectrum changes due to environmental or electrical variations, the original calibration equations may become invalid, causing the measurement accuracy to degrade.

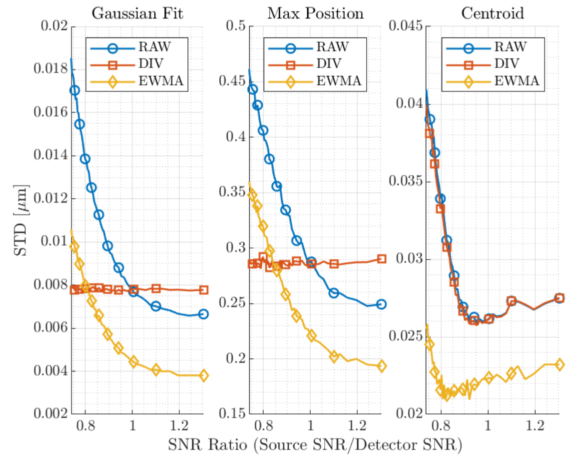

Figure 7: Standard deviation of peak position estimates using different correction strategies across varying ratios of source spectral noise to detector noise. Each subplot corresponds to a different peak detection method.

In addition to systematic errors, we examined how spectral noise influences estimation uncertainty across three peak detection strategies: maximum detection, centroid estimation, and Gaussian fitting. For the maximum-based approach, we derived an analytical formulation to quantify the probability of incorrect peak detection. Furthermore, we extended this analysis to account for non-uniform noise variance across spectral channels, showing how this spatially varying noise affects localization accuracy.

Similar conclusions were drawn by Hagen and Dereniak [39], who analytically derived the dependence of Gaussian peak estimation variance on signal-to-noise ratio and spectral noise characteristics. Yu and Peng [40] further demonstrated that unaccounted asymmetry and structured noise can significantly bias peak localization in experimental data, reinforcing the need for model-aware signal processing in precision sensing applications.

These findings, suggest that if prior information about the illumination spectrum is available, it can be used to predict or even compensate for uncertainty in peak detection. One practical approach is to use a secondary reference spectrometer to monitor the illumination spectrum in real time. This reference can then be used to correct the AIS, thereby improving peak localization accuracy under certain noise conditions.

However, the effectiveness of such compensation strongly depends on several real-world implementation factors:

- The **spectral transfer functions** of the AIS and the reference detection paths must be well-matched – apart from the confocal axial response.
- Both AIS and reference signals must be acquired **synchronously** to ensure valid compensation.
- The **uncorrelated noise** contribution should remain below the intensity fluctuations introduced by the light source.

Dual spectrometer chromatic confocal sensor

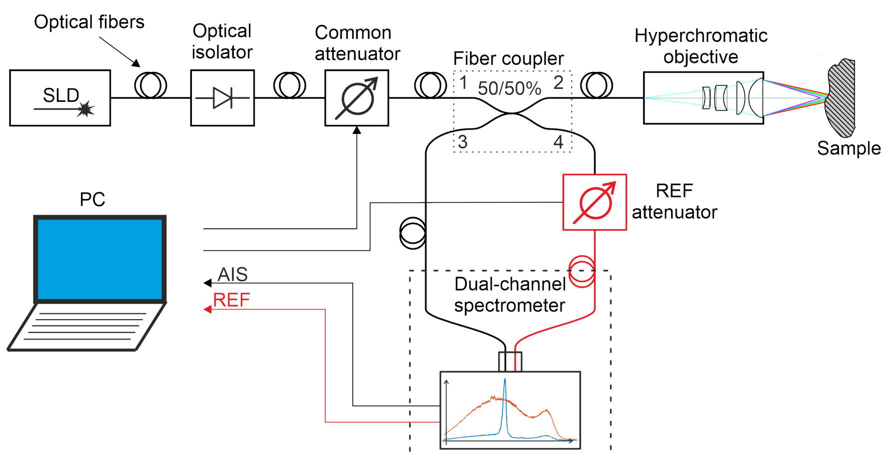

Figure 8: Block diagram of the dual-beam spectrometer layout. Beams are color-coded by wavelength.

If these conditions are not met, compensation may fail or even introduce additional distortion. In the following sections, an experimental system is proposed and validation of the simulated effects through measurements is presented.

3. Experimental system

Based on the simulation results, a custom CC system was developed, building upon a previously proposed configuration utilizing an SLD light source [13]. The new design introduces a dual-beam spectrometer architecture intended to meet the previously defined requirements and enable simultaneous acquisition of the AIS signal and the light source spectrum. This experimental setup was constructed to validate the concept of a reference-compensated CC sensor and to facilitate investigations into signal processing methods aimed at reducing peak localization errors and improving noise resilience. The following experiments were conducted using the test platform:

- Identify and compensate for spectral mismatches between the AIS and reference (REF) channels, originating from mechanical misalignment.
- Investigate the temperature- and current dependent spectral shape variation of the light source and its impact on peak localization accuracy. Compare results with and without reference-based correction.

3.1. Presentation of the custom confocal system with reference path

The block diagram and the actual realization of the extension of the – in [13] presented – prototype system is shown in Figures 8 and 9, highlighting the dual-spectrum acquisition technique. The system is based on a fiber-optic design utilizing a 50:50 fiber splitter (Thorlabs TW850R5A2), which separates the reflected chromatic signal from the illumination beam. In the proposed configuration, the secondary output of the splitter is used to monitor the spectral distribution of the light source.

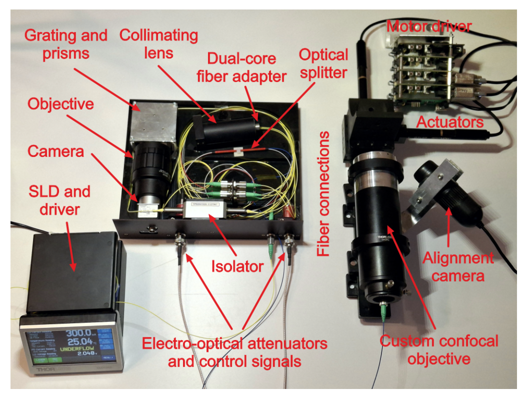

Figure 9: Labeled overview of the dual-channel, fiber-based CC measurement system

The custom confocal objective, consisting of four elements (three custom spherical lenses and one catalog asphere), was designed in Zemax OpticStudio with the following key parameters: an object-space (fiber end) NA of 0.13, an image-space (sample side) NA of 0.4, and a diffraction-limited point spread function (PSF) across the full SLD bandwidth. The objective provides a working distance of 43 mm and an effective focal length of 35.47 mm. According to the sequential optical model, the designed measurement range for the wavelength interval 820 nm to 920 nm is 356.1 µm. The resulting axial sampling resolution, based on the spectrometer dispersion and the detector pixel count, is approximately

$$\frac{356.1\,\mu\text{m}}{2592\text{ pixels}} \approx 0.14\,\mu\text{m/pixel},$$

without the use of sub-pixel interpolation methods such as peak fitting. The lateral resolution of the system is defined by the diffraction-limited spot size according to the Rayleigh criterion and is further enhanced by the double-pass nature of the confocal system:

$$\delta_x(\lambda) = \frac{0.61\lambda}{\text{NA}}, \tag{5}$$

which yields $\delta_x \approx 1.3\,\mu m$ at $\lambda = 860\,nm$. A detailed description of the design process is provided in our previous publication [13].

To ensure effective operation, the temporal delay between the acquisition of the chromatic and reference spectra must be minimal. Using two separate spectrometers complicates this requirement and introduces additional uncertainties. To overcome this challenge, a dual-beam spectrometer architecture was designed and implemented. Figure 10 shows a wireframe ZEMAX model of the optical layout. The dual-beam architecture is realized by combining the fiber ends of the chromatic and reference paths using a custom dual-core fiber adapter, illustrated in the top-left corner of Figure 10. This adapter is mechanically compatible with a standard 1" Thorlabs SM1 lens tube, supporting modular assembly.

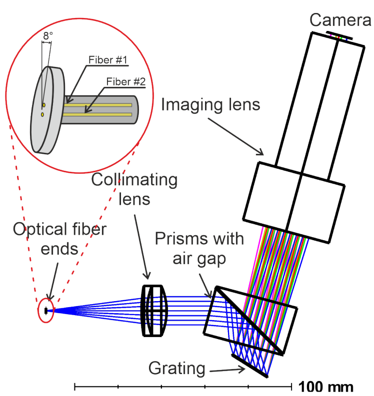

Figure 10: ZEMAX wireframe model of the custom dual-beam spectrometer with front-facing prisms. The dual-core fiber adapter is shown in the top-left corner. Beams are colored by wavelength.

The two beams are collimated and directed toward a reflective diffraction grating. The spectrally separated beams are then projected quasi-telecentrically onto the image sensor using a commercial objective lens (Edmund Optics 86-410). To reduce the optical system's footprint, a Littrow prism assembly is employed. The collimated beams undergo total internal reflection in the first prism and are directed toward the grating. After diffraction, the beams re-enter the prism, but due to the altered angle, they are now refracted instead of reflected, causing additional angular deviation and chromatic dispersion.

To mitigate this undesired effect and allow for compact projection optics, a second, reversed prism is positioned with an air gap parallel to the hypotenuse of the first prism. This configuration realigns the diffracted beams and directs them toward the detector under optimized angles. As the beams are spatially separated in the vertical direction by design, their respective spectra appear as two distinct horizontal traces on the detector, as depicted in Figure 11. By scanning the detector area, the positions of these spectra can be located, and suitable regions of interest (ROIs) can be selected. This method allows for significantly faster acquisition compared to full-frame readouts, enabling measurement speeds in the kHz range. The use of a global shutter camera ensures simultaneous sampling of both spectra. In the prototype system, the chosen device was a Basler ace acA2500-60um camera [41] with a resolution of 2048x2592 pixels.

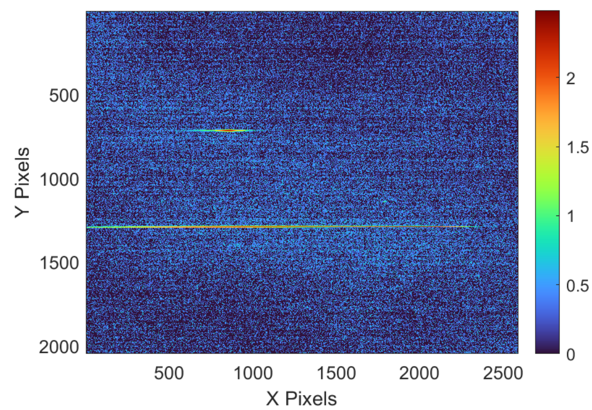

Figure 11: Logarithmically scaled raw detector image acquired using the dual-beam spectrometer. The high-intensity spectral line from the reference path and the AIS signal are clearly distinguishable.

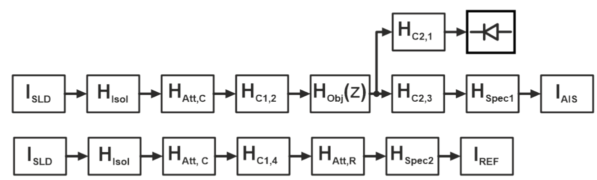

Figure 12: Signal path model of AIS and REF channels.

The signal path model is illustrated in Figure 12. Labels in the figure follow a convention where **I** denotes a spectral signal and **H** represents a wavelength-dependent optical transfer function, parameterized by λ:

- I_{SLD} – SLD spectrum
- I_{AIS} – AIS spectrum
- I_{REF} – Reference spectrum
- H_{Isol} – Optical isolator
- $H_{\mathrm{Att,C}}$ – Attenuator in the common path
- $H_{\mathrm{Att,R}}$ – Attenuator in the reference path
- $H_{\mathrm{C}i,j}$ – Coupling efficiency from port i to port j
- H_{Obj} – Confocal response
- $H_{\mathrm{Spec},n}$ – Wavelength-to-pixel mapping function of the spectrometers, including aberrations and nonlinearities

As the model suggests, fully accounting for the complexity of the physical system–especially the transfer functions'

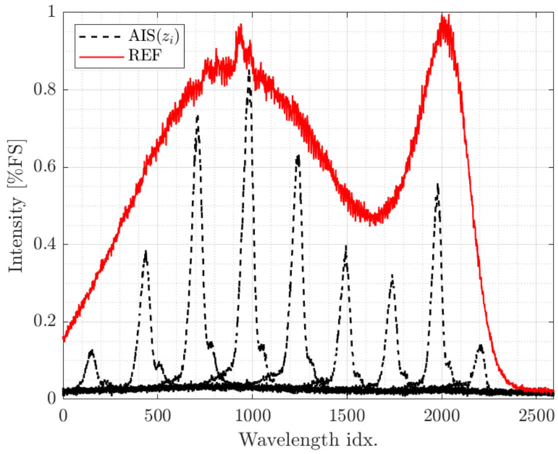

Figure 13: Captured AIS and REF signals at different z_i positions using the proposed dual-channel system.

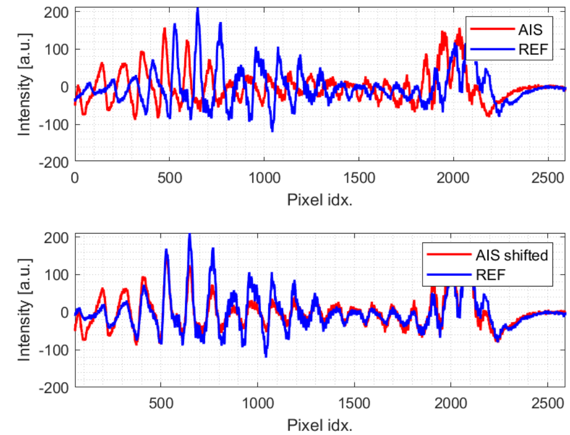

Figure 14: Spectral alignment of the two channels using high-frequency components and cross-correlation analysis.

sensitivity to drift, setpoints, and environmental conditions– is beyond the scope of this work. Nevertheless, several key factors must be addressed: the channels must be matched in both wavelength and sensitivity, and compensation must be continuously adapted to track potential drifts and setpoint-dependent variations. Despite these challenges and the necessary simplifications in our analysis, the observed improvements in accuracy demonstrate the promise of the proposed approach for broader application in spectral sensing systems.

3.2. Channel matching

Due to mechanical misalignment, the two spectrometer channels do not necessarily correspond to the same wavelength at a given horizontal pixel index. Figure 13 shows raw measurement data captured by the dual-beam system at various sample distances z_i without any post-processing. Both spectral misalignment and gain mismatch between the channels are evident. To compensate for these effects, a calibration measurement was performed by directly connecting the optical fiber – originally guiding light into the CC objective – into the AIS spectrometer arm. In this configuration, the two spectral responses can be matched, aside from discrepancies caused by the non-ideal transmission characteristics of the optical components.

To eliminate the influence of such gain discrepancies, the low-frequency components (i.e., slowly varying intensity across the spectrum) were filtered out, preserving only the high-frequency spectral transitions. By computing the cross-correlation of the filtered signals, the pixel-wise wavelength offset between the two channels was estimated from the location of the correlation peak. This offset can then be used to transform one spectral channel into the base of the other. In the prototype system, the estimated horizontal offset required to align the AIS channel with the REF channel was found to be 55 pixels. This value was applied during the evaluation measurements to align the spectra. Figure 14 shows the high-frequency components of both spectra before and after alignment.

The compensation method applied in this work was a simple pixel-by-pixel division, preceded by boxcar moving-average filtering of the spectra. In selected test cases, exponential temporal averaging was also implemented in order to assess how averaging alone reduces measurement noise in the absence of reference compensation. These tests indicated that exponential filtering can outperform pixel-wise division in suppressing random noise; however, it is not capable of mitigating systematic errors arising from spectral shape drifts. Additionally, temporal averaging reduces the effective sampling rate in proportion to the filter time constant.

3.3. Effect of SLD spectral shape variations

The impact of spectral shape variations of the light source was investigated by modulating the temperature and drive current of the SLD. These parameters were controlled via the built-in Peltier element and current driver of the SLD module (Thorlabs CLD1015).

For the current drift measurement, five different current setpoints were selected. At each setpoint, 1000 spectra were collected at a frame rate of 1 kHz while a mirror was translated across the focal range of the objective lens using a high-precision actuator (Thorlabs Z812B). A total of 100 discrete distance steps were evaluated, covering a focal range of ~~approximately~~ 300 μm. The peak position of each spectrum was determined using a Gaussian fitting method, and the results were averaged. Measurement data acquired at a single distance step for different drive current setpoints are shown in Figure 15. A non-linear effect of varying the drive current is evident: the intensity of the secondary peak decreases as the current decreases, while the main lobe remains largely unaffected. The differences in the estimated peak positions between the current setpoints were then calculated for each distance step. Additional signal smoothing was applied on the results by a moving average filter the tap length of 5 in order to highlight only the slowly varying component of the peak position error, that is directly related to the spectral distortion.

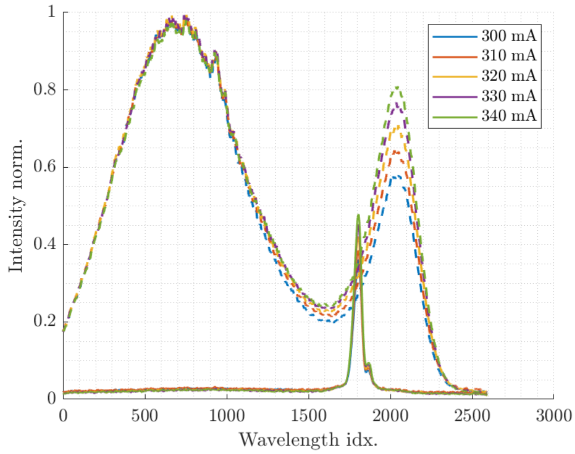

Figure 15: Spectral shape drift induced by SLD drive current variation. The data show both the REF (dashed) and AIS (solid) signals at a selected distance index. A non-linear effect is evident: the main lobe remains largely intact, while the intensity of the secondary peak changes significantly with drive current.

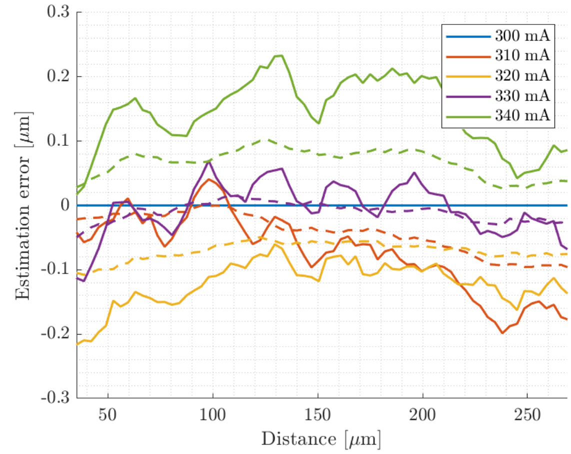

Figure 16: Estimated peak position differences between the nominal and other current setpoints. Dashed curves represent the reference-compensated results for the corresponding setpoints. The dataset measured at 300 mA was used as the baseline for comparison.

Figure 16 presents the peak estimation errors for both the raw (uncorrected) and the reference-compensated signals. The compensation reduced the error by 57.3%, calculated as the relative reduction in the mean estimation error across the full distance range when comparing the compensated and non-compensated results.

The same procedure was repeated while varying the SLD temperature. Figure 17 shows the spectral shape variation induced by temperature drift, with the data smoothed using a moving average filter of tap length five. In this case, non-linear spectral shape changes are again evident; however, the most pronounced effect is the variation in the intensity of the main lobe. The corresponding estimation error is presented in Figure 18. The results are consistent with those of the current sweep measurements, further supporting the validity of the proposed compensation technique.

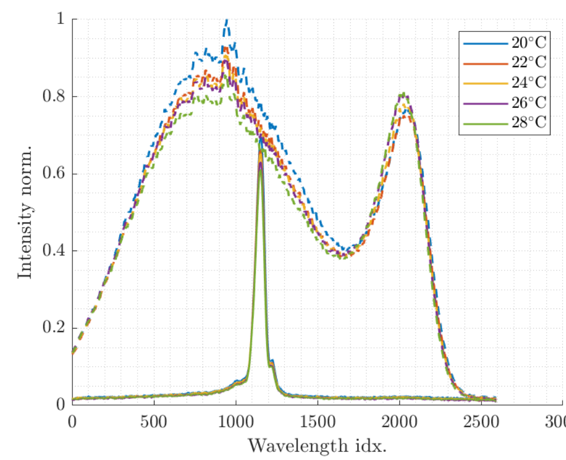

Figure 17: Spectral shape drift caused by SLD temperature variation. The data show both the REF (dashed) and AIS (solid) signals at a selected distance index.

3.4. Denoising performance

As suggested in the simulation section, a denoising approach was applied using information from the reference channel, and the results were compared to evaluations based solely on the AIS signal. A standard microscopy glass slide was translated continuously through the focal range of the objective using a linear actuator, moving at ~~approximately~~ 35 µm s^{-1}. A total of 10,000 spectral samples were captured at a rate of 1 kHz, resulting in 10 seconds of measurement time. During this period, the stage traveled across the full 350 µm focal range of the confocal objective.

The captured data was processed in MATLAB using the same peak detection framework described in the simulation section. Raw AIS data was analyzed using both a simple maximum detection method and a refined Gaussian fitting procedure based on Caruana's algorithm. The peak estimation algorithm proceeded as follows:

1. Detect the peak intensity and corresponding spectral index using the maximum of the AIS signal.
2. Store the wavelength index corresponding to the detected maximum as the result of the simple peak detection.
3. For Gaussian fitting:
   (a) Apply a threshold of $I_{\text{thr}} = 0.5 \cdot I_{\max}$ to select points above half of the peak intensity.
   (b) Extract the corresponding wavelength and intensity vectors, λ_{fit} and y_{fit}.
   (c) Perform Gaussian fitting on the subset $\{\lambda_{\text{fit}}, y_{\text{fit}}\}$ using Caruana's method.
   (d) Store the centroid μ_{AIS} of the fitted Gaussian as the peak estimate.

To evaluate peak estimation accuracy, a second-order polynomial was fitted to the nominal distance sweep to

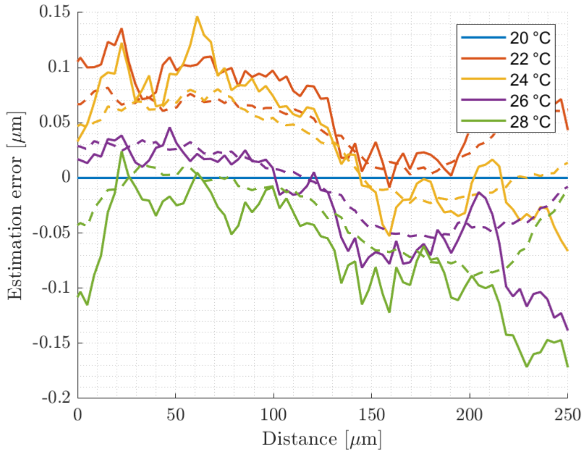

Figure 18: Estimated peak position differences between the nominal and other temperature setpoints. Dashed curves represent the reference-compensated results for the corresponding setpoints. The dataset measured at 20°C was used as the baseline for comparison.

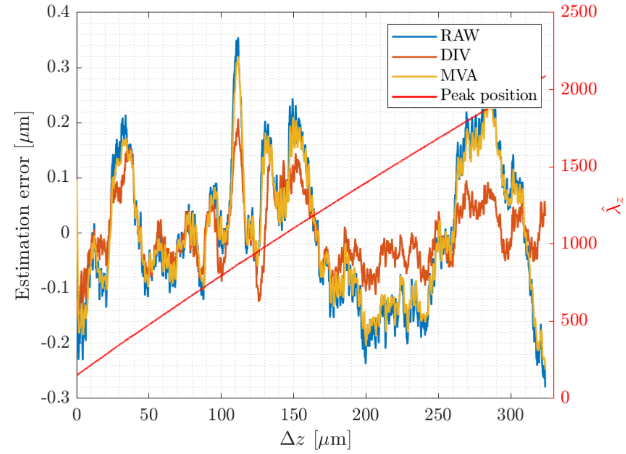

Figure 19: Estimated peak position fluctuations across the focal range acquired over 10,000 steps. Only the central 8,000 samples are shown due to edge artifacts. The detected absolute peak position is plotted on the secondary y-axis.

remove the deterministic trend, and residuals were analyzed to determine the estimation error and standard deviation. This analysis was performed on the raw AIS signal, the AIS signal after exponential moving average filtering, and the divided (reference-compensated) signal (DIV). The results showed a minor but consistent improvement in peak estimation stability with the reference-based compensation. Specifically, the standard deviation of the de-trended peak position across the full scan range was 0.1717 µm for the raw AIS signal, 0.1699 µm for the MVA-filtered signal, and 0.1346 µm for the DIV signal using Gaussian fitting.

Figure 19 shows the measured peak fluctuations across the focal range, evaluated using the Gaussian fitting method. The three curves correspond to different processing schemes: the raw AIS signal without compensation, the division-by-reference compensation (DIV), and the exponentially moving-averaged AIS spectrum (MVA) with a time constant of $\tau = 0.9$. For reference, the secondary y-axis indicates the estimated absolute peak position of the raw signal across the focal range.

Additional tests were performed on practical samples with very low reflectivity, including microstructured and unprocessed black rubber surfaces, as well as an MgF2 antireflection-coated glass window (Edmund Optics #17-173). The samples were attached to a microscopy slide using double-sided adhesive and mounted on the actuator stage. During the measurements, the beam was focused on the sample surfaces, and optical attenuators were adjusted to achieve an appropriate signal level. Data were acquired at a sampling rate of 1 kHz, recording 10 000 spectra for each case. Images of the samples are shown in Figure 20.

The recorded spectra were evaluated using both Gaussian peak fitting and simple maximum detection, with and without reference compensation. As a pre-processing step, pixel-wise smoothing was applied using a moving average

Figure 20: Test samples used to evaluate the performance of the prototype system on real-life specimens, imaged with a microscope camera attached to the measurement setup. From left to right: a microstructured surface of an elastomer seal, the flat surface of the same elastomer seal, and an antireflection-coated optical window. The focused infrared beam of the microscope is visible on the surface of the central (flat elastomer) sample.

filter with a tap length of five. Finally, the residual errors from the 10 000 measurements were calculated and are presented as histograms in Figure 21.

Figure 22 presents the captured signal from the three different samples. Reasonable signal levels could be achieved even on the lowest reflecting surfaces; however, due to stray light, the spectrum of the light source starts to appear as background. It requires a dark compensation by capturing a dark signal out of focus and subtracting it from the measured data; however, here we must also consider the drift of the dark signal. This could be followed with the reference channel, by capturing the reference signal as well, by the

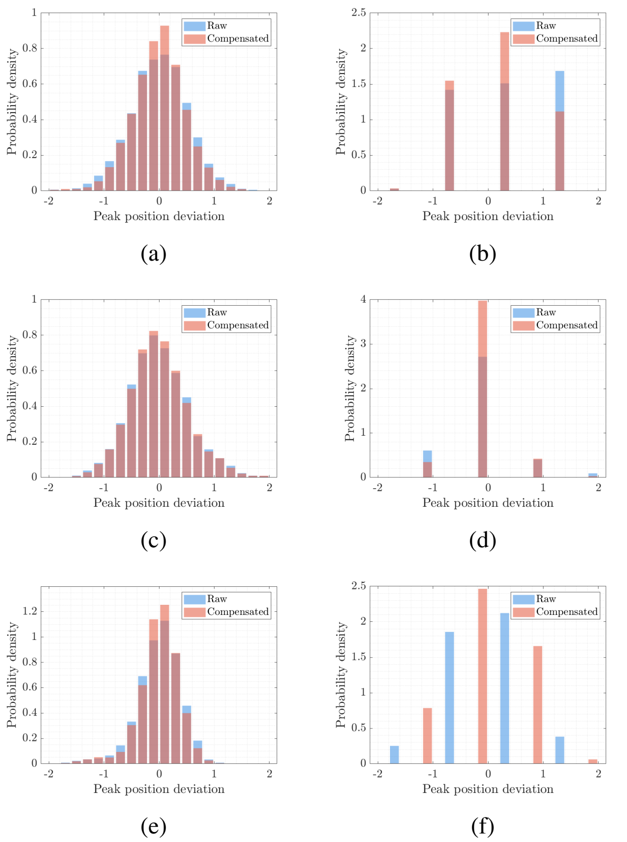

Figure 21: Histogram of the peak estimation error for the three low-reflectivity samples shown in Figure 20, evaluated using the Gaussian peak fitting method (a, c, e) and the maximum detection technique (b, d, f). Peak position deviation is expressed in detector pixels with a full scale range of 2592 bins. Each row corresponds to a specific sample in the following order: structured rubber surface, flat rubber surface, and antireflection-coated glass window. For both signal processing techniques, the histograms clearly demonstrate the reduced variance achieved by applying reference-channel compensation.

acquisition of the dark, and performing the compensation of the dark signal with the distortion of the references as well.

Figure 23 displays the surface topography of the structured and flat rubber surfaces, obtained by two-dimensional scanning of a 1 mm^2 area with lateral steps of 10 µm using the prototype system.

It should be noted, however, that the reference channel can introduce additional noise if the spectral alignment is inaccurate, or a significant gain mismatch between the channels is present. This limitation is recognized in the current design and motivates the development of a more advanced signal processing approach that can estimate the correlation strength of the noise components in the AIS and REF channels, and apply normalization weighted by this correlation. Addressing this issue represents a major priority in the upcoming research phase, together with the migration of the signal processing to a DSP or FPGA platform in order to reduce the computational load on the host PC in case of a more complex signal processing algorithm is applied.

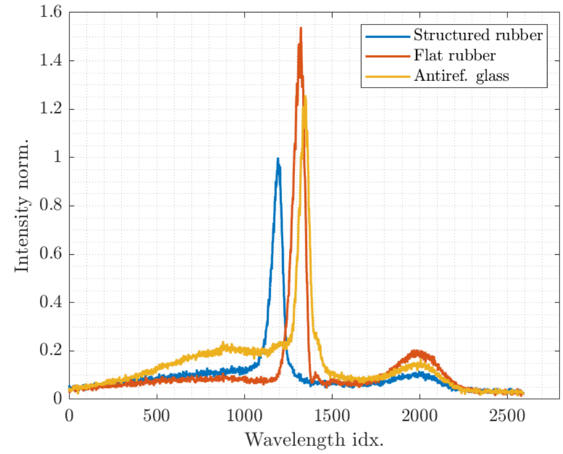

Figure 22: Captured AIS signals from the three samples. A distinct peak is observable in each case; however, at higher signal intensities a background contribution appears, originating from scattering within the optical components. This background can be effectively removed by performing a proper dark-signal acquisition prior to measurement.

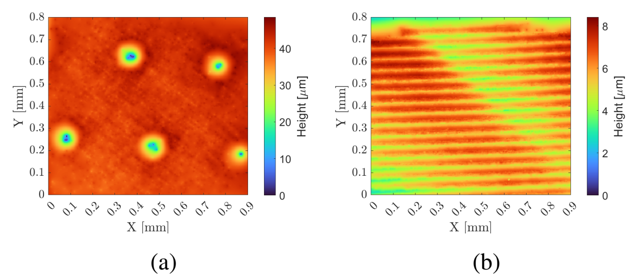

Figure 23: Surface topography of the flat- and structured side of the rubber samples captured by the prototype system.

3.5. Computational complexity and processing speed

As the proposed system incorporates an additional channel for compensation, both the signal processing workload and the data rate are effectively doubled. The computational complexity of the compensation and peak estimation procedure nevertheless scales linearly with the number of spectral samples, i.e. $\mathcal{O}(N)$ with $N = 2592$. For each acquired spectrum, the following operations are carried out:

- Pixel-wise normalization of the AIS channel by the REF channel requires 2.6×10^3 floating-point divisions.
- Thresholding of the normalized spectrum, involving an additional 2.6×10^3 comparisons.
- Gaussian peak estimation using Caruana's moment-based algorithm, which reduces to the calculation of weighted sums (mean, variance, amplitude) across the selected pixels, requiring on the order of 5×10^3–1×10^4 multiplications and additions.

The total computational effort per spectrum is therefore 2×10^4 floating-point operations. At the present acquisition rate of 925 Hz, this corresponds to a sustained requirement of about $2{\times}10^7$ FLOP/s. This load is negligible compared to the capacity of a modern PC CPU core, which typically sustains 10^9–10^{10} FLOP/s. Consequently, the real-time implementation of the simple pixel-wise division technique on a conventional PC is not limited by computational performance. However, the application of more sophisticated correlation-based estimators may present challenges even for high-end PCs. In this context, dedicated signal processing hardware can offer significant advantages. For example, a floating-point digital signal processor (DSP) with a throughput in the low GFLOP/s range is capable of sustaining processing rates on the order of 10^4 spectra per second, which is well above the current measurement rate. An FPGA directly interfaced with the spectrometer sensor is particularly attractive: normalization and thresholding can be implemented as a streaming pipeline, while Gaussian parameter estimation reduces to a set of parallel accumulators for moment calculations. Such a design enables fully pipelined operation with latencies on the order of microseconds per spectrum. Moreover, FPGA or DSP implementations allow only the extracted peak parameters to be transmitted to the host, thereby reducing both computational load and data bandwidth requirements. This architecture is thus highly suitable for future integration of the proposed compensation method in compact, embedded measurement systems.

4. Conclusion

In this work, we presented an upgraded version of a previously proposed custom chromatic confocal measurement system that enhances peak localization accuracy by compensating for spectral drift and fluctuations using a synchronized reference channel. The system incorporates a custom dual-channel spectrometer to monitor and correct measurement errors caused by variations in the light source spectrum in real time.

Simulations were conducted to analyze the impact of signal distortion and noise on peak localization accuracy. The study demonstrated that normalizing the measured signal with the reference spectrum can reduce the influence of source instability on the measurement results. Mathematical analysis showed how noise in the spectral signal affects peak estimation accuracy and how uneven noise distribution introduces bias.

Experimental validation confirmed that the proposed compensation method improves measurement robustness, reducing peak position errors by up to 20% under both slow drift and high-speed acquisition conditions.

These findings confirm that spectral referencing is an effective and practical method for enhancing the accuracy and stability of spectrally encoded distance measurements. Future work may focus on optimizing correlation-based denoising filters and implementing real-time processing on embedded platforms.

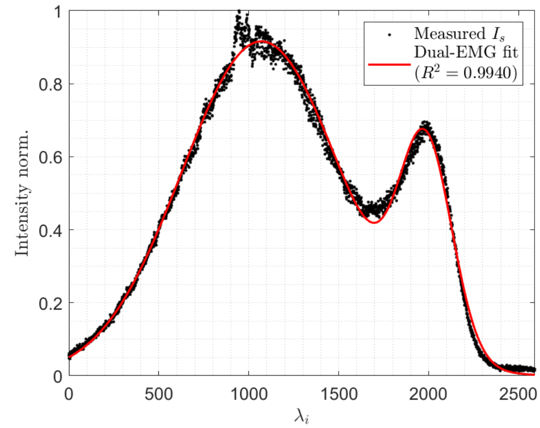

Figure 24: Example result of fitting the dual-peak exponentially modified Gaussian model to a measured light source spectrum. The asymmetry and secondary lobe are accurately captured.

Acknowledgment

The research reported in this paper was supported by the Budapest University of Technology and Economics and Optimal Optik Ltd. The research was also supported by the Hungarian National Research, Development and Innovation (NRDI) Office under the Cooperative Doctoral Programme for Doctoral Scholarship (KDP-2021) and by the János Bólyai Research Grant (BO/0042/23/6) of the Hungarian Academy of Sciences.

Appendix A: Dual-peak exponentially modified Gaussian model and fitting procedure

To model the light source spectra, we use a composite function consisting of an exponentially modified Gaussian (EMG) peak and a secondary symmetric Gaussian peak. The EMG captures asymmetrically broadened features typical of spontaneous emission processes, while the Gaussian accounts for the secondary lobe.

The full mathematical expression is given in Equation A-1, where parameters μ_0, a_0, σ_0, and τ define the EMG component, and a_1, $\Delta\mu$, and σ_1 describe the secondary Gaussian. This model is implemented in MATLAB through the function `dualEmgF`, which evaluates the sum of an EMG and a Gaussian at each input point. The fitting process begins with a simplified version using only the EMG component, implemented in `EMG_Fit`. It estimates the initial parameters by locating the signal maximum and measuring the spectral width. Optimization is performed using MATLAB's `lsqcurvefit`, with parameter bounds that allow both positive and negative exponential decay constants (τ), enabling modeling of left- or right-skewed peaks. Figure 24 illustrates the dual-Gaussian fitting results applied to a representative spectrum captured from the reference channel.

$$y(x) = \underbrace{\left(\frac{a_0\sigma_0}{|\tau|}\sqrt{\frac{\pi}{2}}\right)\exp\left(\frac{\sigma_0^2}{2\tau^2} - \frac{x-\mu_0}{\tau}\right)\cdot \operatorname{erfc}\left(\frac{\sigma_0}{|\tau|\sqrt{2}} - \frac{(x-\mu_0)}{\sigma_0\sqrt{2}}\cdot \operatorname{sign}(\tau)\right)}_{\text{Exponentially Modified Gaussian (EMG)}} + \underbrace{a_1\cdot\exp\left(-\frac{(x-\mu_0-\Delta\mu)^2}{2\sigma_1^2}\right)}_{\text{Gaussian peak}}. \quad \text{(A-1)}$$

Appendix B: Probability that a given Gaussian variable is the maximum

Let $X_1, X_2, \dots, X_N$ be independent Gaussian random variables:

$$X_i \sim \mathcal{N}(\mu_i, \sigma_i^2), \quad \text{for } i = 1, \dots, N. \quad \text{(B-1)}$$

We are interested in computing the probability that a specific variable X_k attains the maximum value among all:

$$P\left(X_k = \max\{X_1, X_2, \dots, X_N\}\right). \quad \text{(B-2)}$$

Since the variables are independent, the probability that X_k is greater than all other variables X_j for $j \neq k$ can be expressed as:

$$P\left(X_k = \max_i X_i\right) = \int_{-\infty}^{\infty} f_k(t) \prod_{\substack{j=1\\ j\neq k}}^{N} F_j(t)\,dt, \quad \text{(B-3)}$$

where $f_k(t)$ is the probability density function (PDF) of X_k, and $F_j(t)$ is the cumulative distribution function (CDF) of X_j, which can be expressed as, respectively:

$$f_k(t) = \frac{1}{\sqrt{2\pi}\sigma_k}\exp\left(-\frac{(t-\mu_k)^2}{2\sigma_k^2}\right), \quad \text{(B-4)}$$

$$F_j(t) = \frac{1}{2}\left[1 + \operatorname{erf}\left(\frac{t-\mu_j}{\sqrt{2}\sigma_j}\right)\right]. \quad \text{(B-5)}$$

The integral in (B-3) represents the probability that X_k takes on a specific value t and all other variables are less than t. After evaluating Equation (B-3) for each $k = 1, \dots, N$ yields the full distribution over which variable is most likely to attain the maximum.

Although no closed-form solution exists in the general case, this expression can be evaluated numerically using quadrature methods or approximated using a Monte Carlo simulation.

Appendix C: Probability of maximum selection in the correlated case

The following multivariate Gaussian vector is considered

$$\mathbf{X} = [X_1, X_2, \dots, X_N]^\top \sim \mathcal{N}(\boldsymbol{\mu}, \boldsymbol{\Sigma}), \quad \text{(C-1)}$$

where $\boldsymbol{\mu} \in \mathbb{R}^N$ is the mean vector and $\boldsymbol{\Sigma} \in \mathbb{R}^{N\times N}$ is the covariance matrix, which may include nonzero off-diagonal elements representing correlations between the variables. The probability that a specific component X_k is the maximum among all components can be written as

$$P\left(X_k = \max\{X_1, X_2, \dots, X_N\}\right). \quad \text{(C-2)}$$

This is equivalent to evaluating the probability that $X_k > X_j$ for all $j \neq k$, which we denote as the event A_k:

$$A_k = \{X_k > X_j \ \ \forall j \neq k\}. \quad \text{(C-3)}$$

The following linear transformation is defined $\mathbf{Z}_k = \mathbf{C}_k\mathbf{X}$, where $\mathbf{C}_k \in \mathbb{R}^{(N-1)\times N}$ is a matrix that computes the set of differences $X_k - X_j$ for all $j \neq k$. Specifically,

$$\mathbf{C}_k = \begin{bmatrix} \mathbf{e}_k^\top - \mathbf{e}_1^\top \\ \vdots \\ \mathbf{e}_k^\top - \mathbf{e}_{k-1}^\top \\ \mathbf{e}_k^\top - \mathbf{e}_{k+1}^\top \\ \vdots \\ \mathbf{e}_k^\top - \mathbf{e}_N^\top \end{bmatrix}, \quad \text{(C-4)}$$

where $\mathbf{e}_i$ is the ith standard basis vector in $\mathbb{R}^N$. The transformed vector $\mathbf{Z}_k$ is itself Gaussian:

$$\mathbf{Z}_k \sim \mathcal{N}(\mathbf{C}_k\boldsymbol{\mu}, \mathbf{C}_k\boldsymbol{\Sigma}\mathbf{C}_k^\top). \quad \text{(C-5)}$$

Then, the desired probability is given by the probability that all components of $\mathbf{Z}_k$ are positive:

$$\begin{aligned} P(X_k = \max X_i) &= P(\mathbf{Z}_k > 0) \\ &= \int_{\mathbb{R}_+^{N-1}} \mathcal{N}\left(\mathbf{z};\, \mathbf{C}_k\boldsymbol{\mu},\, \mathbf{C}_k\boldsymbol{\Sigma}\mathbf{C}_k^\top\right) d\mathbf{z}, \end{aligned} \quad \text{(C-6)}$$

Equation (C-6) represents the orthant probability of a multivariate normal distribution, which generally has no closed-form solution for $N > 3$, but can be efficiently evaluated using specialized numerical algorithms such as those proposed by Genz and Bretz [34], or approximated by Monte Carlo integration.

Figure 25 compares simulation results obtained using Monte Carlo integration and Genz's method for a synthetically generated Töplitz covariance matrix. When the evaluation of the integral is restricted to a finite number of wavelength bins around the true peak region, the computation can be completed within a reasonable processing time while still providing a good agreement with the Monte Carlo results.

CRediT authorship contribution statement

Lóránt Tibor Csőke: Conceptualization of this study, Methodology, Signal processing. **Szabolcs Károly Kautny:** Mechanical and optical design, Conceptualization. **Zsolt Kollár:** Writing - Review & Editing.

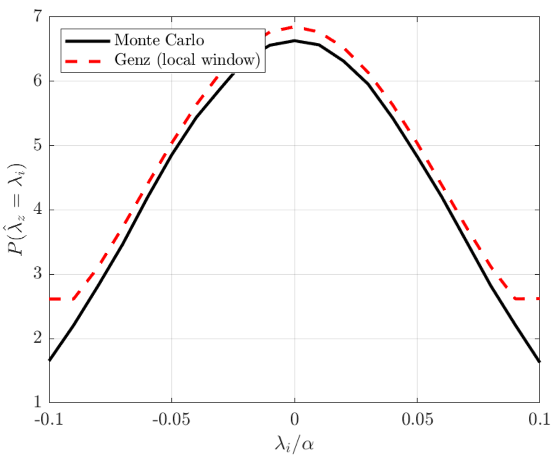

Figure 25: Validation of the analytical derivation via Monte Carlo simulation with 10^6 trials. A synthetic covariance matrix with exponentially decaying correlation was used, generated as $\Sigma_L = \sigma^2 \cdot \text{toeplitz}(\rho^{0:N_\lambda-1})$. The Genz integral was evaluated within a ± 10 bin region around the true peak location.

Declaration of generative AI and AI-assisted technologies in the writing process

During the preparation of this work, the authors used [Grammarly, OpenAI-ChatGPT] to improve readability and language. After using these tools, the authors reviewed and edited the content as needed and take full responsibility for the content of the publication.

References

[1] Z. Zhang, R. Lu, A. Zhang, H. Li, J. Liu, Monochromatic led-based spectrally tunable light source for chromatic confocal sensors, Optical Engineering 62 (2023).

[2] C. Liu, G. Lü, C. Liu, D. Liu, Compact chromatic confocal sensor for displacement and thickness measurements, Measurement Science and Technology 34 (2023) 055104.

[3] J. Bai, J. Li, X. Wang, Q. Zhou, K. Ni, X. Li, A new method to measure spectral reflectance and film thickness using a modified chromatic confocal sensor, Optics and Lasers in Engineering 154 (2022) 107019.

[4] J. Bai, Y. Wang, X. Wang, Q. Zhou, K. Ni, X. Li, Three-probe error separation with chromatic confocal sensors for roundness measurement, Nanomanufacturing and Metrology 4 (2021) 247–255.

[5] W. Kapłonek, M. Sutowska, M. Ungureanu, K. Çetinkaya, Optical profilometer with confocal chromatic sensor for high-accuracy 3d measurements of the uncirculated and circulated coins, Journal of Mechanical and Energy Engineering 2 (2018) 181–192.

[6] P. Chiariotti, M. Fitti, P. Castellini, S. Zitti, M. Zannini, N. Paone, Smart quality control station for non-contact measurement of cylindrical parts based on a confocal chromatic sensor, Ieee Instrumentation and Measurement Magazine 21 (2018) 22–28.

[7] Q. Yu, Y. Zhang, W. Shang, S. Dong, C. Wang, Y. Wang, T. Liu, C. Fang, Thickness measurement for glass slides based on chromatic confocal microscopy with inclined illumination, Photonics 8 (2021) 170.

[8] C. Olsovsky, R. Shelton, O. Carrasco-Zevallos, B. E. Applegate, K. C. Maitland, Chromatic confocal microscopy for multi-depth imaging of epithelial tissue, Biomed. Opt. Express 4 (2013) 732–740.

[9] M. Hillenbrand, L. Lorenz, R. Kleindienst, A. Grewe, S. Sinzinger, Spectrally multiplexed chromatic confocal multipoint sensing, Optics Letters 38 (2013) 4694.

[10] M. Taphanel, B. Hovestreydt, J. Beyerer, Speed-up chromatic sensors by optimized optical filters, in: P. H. Lehmann, W. Osten, A. Albertazzi (Eds.), Optical Measurement Systems for Industrial Inspection VIII, volume 8788, International Society for Optics and Photonics, SPIE, 2013, p. 87880S. URL: https://doi.org/10.1117/12.2020387. doi:10.1117/12.2020387.

[11] S. Dobson, P. Sun, Y. Fainman, Diffractive lenses for chromatic confocal imaging, Applied Optics 36 (1997) 4744.

[12] M. Hillenbrand, R. Weiss, C. Endrödy, A. Grewe, M. Hoffmann, S. Sinzinger, Chromatic confocal matrix sensor with actuated pinhole arrays, Appl. Opt. 54 (2015) 4927–4936.

[13] L. T. Csőke, S. Kautny, L. Domján, G. Szarvas, L. Lugosi, A. Csákányi, Z. Kollár, Development and validation of a surface profiling system for end of line monitoring of microstructured elastomer seals based on chromatic confocal microscopy, Precision Engineering 77 (2022) 365–374.

[14] V. Shidlovski, Superluminescent diodes, Application Notes, 2004. URL: http://www.superlumdiodes.com, principles of SLD operation. SLD output power. SLD spectrum and coherence. SLD and optical feedback. Temperature performance of SLDs. SLD spatial characteristics. SLD reliability and lifetime. Driving of SLDs. Stability of SLD operation.

[15] M. Xi, H. Liu, D. Li, Y. Wang, Spectral signal asymmetry analysis and encoding of chromatic confocal sensors, IEEE Sensors Journal 24 (2024) 1953–1962.

[16] M. Xi, H. Liu, D. Li, Y. Wang, Intensity response model and measurement error compensation method for chromatic confocal probe considering the incident angle, Optics and Lasers in Engineering 172 (2024) 107858.

[17] N. He, H. Hu, Z. Cui, X. Xu, D. Zhou, Y. Chen, P. Gong, Y. Chen, C. Kuang, Compact chromatic confocal lens with large measurement range, Sensors 24 (2024).

[18] C. Chen, W. Yang, J. Wang, W. Lu, X. Liu, X. Jiang, Accurate and efficient height extraction in chromatic confocal microscopy using corrected fitting of the differential signal, Precision Engineering 56 (2019) 447–454.

[19] W. Lu, C. Chen, J. Wang, R. Leach, C. Zhang, X. Liu, Z. Lei, W. Yang, X. J. Jiang, Characterization of the displacement response in chromatic confocal microscopy with a hybrid radial basis function network, Opt. Express 27 (2019) 22737–22752.

[20] W. Lu, C. Chen, H. Zhu, J. Wang, R. Leach, X. Liu, J. Wang, X. Jiang, Fast and accurate mean-shift vector based wavelength extraction for chromatic confocal microscopy, Measurement Science and Technology 30 (2019) 115104.

[21] G. A. Alphonse, Design of high-power superluminescent diodes with low spectral modulation, in: N. K. Dutta, R. W. Herrick, A. K. Chin, N. K. Dutta, R. W. Herrick, K. J. Linden, D. J. McGraw (Eds.), Test and Measurement Applications of Optoelectronic Devices, volume 4648, International Society for Optics and Photonics, SPIE, 2002, pp. 125 – 138. URL: https://doi.org/10.1117/12.462649. doi:10.1117/12.462649.

[22] J. Park, X. Li, Theoretical and numerical analysis of superluminescent diodes, Journal of Lightwave Technology 24 (2006) 2473–2480.

[23] M. Rossetti, J. Napierala, N. Matuschek, U. Achatz, M. Duelk, C. Vélez, A. Castiglia, N. Grandjean, J. Dorsaz, E. Feltin, Superluminescent light emitting diodes: the best out of two worlds, in: H. Schenk, W. Piyawattanametha, W. Noell (Eds.), MOEMS and Miniaturized Systems XI, volume 8252, International Society for Optics and Photonics, SPIE, 2012, p. 825208. URL: https://doi.org/10.1117/12.912759. doi:10.1117/12.912759.

[24] Thorlabs, Inc., IO-F-SLD150-895 Fiber Isolator Manual, Thorlabs, 2025. URL: https://www.thorlabs.com/drawings/8781e4c9791cc16b-141C6AFE-E67F-D9B3-05AA02B051FBE17D/IO-F-SLD150-895-Manual.pdf, accessed: 2025-04-29.

[25] A. Yurek, L. Goldberg, J. Weller, H. Taylor, Fringe visibility and phase noise in superluminescent diodes, IEEE Journal of Quantum Electronics 23 (1987) 1256–1260.

[26] H. Taylor, Intensity noise and spontaneous emission coupling in superluminescent light sources, IEEE Journal of Quantum Electronics 26 (1990) 94–97.
[27] T. Liu, J. Wang, Q. Liu, J. Hu, Z. Wang, C. Wan, S. Yang, Chromatic confocal measurement method using a phase fresnel zone plate, Opt. Express 30 (2022) 2390–2401.
[28] B. Richards, E. Wolf, Electromagnetic diffraction in optical systems. ii. structure of the image field in an aplanatic system, Proceedings of the Royal Society of London. Series A. Mathematical and Physical Sciences 253 (1959) 358–379.
[29] T. R. Corle, C.-H. Chou, G. S. Kino, Depth response of confocal optical microscopes, Opt. Lett. 11 (1986) 770–772.
[30] T. Wilson, C. Sheppard, Theory And Practice Of Scanning Optical Microscopy, volume -1, Academic Press, 1984.
[31] M. A. Browne, O. Akinyemi, A. Boyde, Confocal surface profiling utilizing chromatic aberration, Scanning 14 (1992) 145–153.
[32] C. Chen, J. Wang, C. Zhang, W. Lu, X. Liu, Z. Lei, W. Yang, X. J. Jiang, Influence of optical aberrations on the peak extraction in confocal microscopy, Optics Communications 449 (2019) 24–32.
[33] H. Guo, A simple algorithm for fitting a gaussian function, IEEE Signal Processing Magazine 28 (2011) 134–137.
[34] A. Genz, F. Bretz, Computation of multivariate normal and *t* probabilities, Lecture Notes in Statistics 195 (2009).
[35] A. Genz, G. Trinh, Numerical computation of multivariate normal probabilities using bivariate conditioning, in: R. Cools, D. Nuyens (Eds.), Monte Carlo and Quasi-Monte Carlo Methods, Springer International Publishing, Cham, 2016, pp. 289–302.
[36] M. Blazek, S. Hartmann, A. Molitor, W. Elsaesser, Unifying intensity noise and second-order coherence properties of amplified spontaneous emission sources, Optics Letters 36 (2011) 3455–3457.
[37] A. Yurek, H. Taylor, L. Goldberg, J. Weller, A. Dandridge, Quantum noise in superluminescent diodes, IEEE Journal of Quantum Electronics 22 (1986) 522–527.
[38] Thorlabs, Inc., TW850R5A2 850nm fiber-coupled pump laser spec sheet, https://www.thorlabs.com/drawings/519f2faf12c95311-78A9AF52-DE95-DC40-8515E2B6203FD1B9/TW850R5A2-SpecSheet.pdf, 2025. Accessed June 21, 2025.
[39] N. Hagen, M. Kupinski, E. L. Dereniak, Gaussian profile estimation in one dimension, Applied Optics 46 (2007) 5374–5383.
[40] Y. Yu, P. Peng, Improved peak detection and quantification of mass spectrometry data by using a bi-gaussian mixture model, BMC Bioinformatics 11 (2010) 1–10.
[41] Basler AG, Basler ace acA2500-60um – Monochrome USB 3.0 Camera, https://www.baslerweb.com/en/shop/aca2500-60um/, 2025. Accessed: 2025-06-24.